Minimalist Model Systems Reveal Similarities and Differences between Membrane Interaction Modes of MCL1 and BAK*

Olatz Landeta[‡1,2], Ane Landajuela[‡1], Ana Garcia-Saez[§¶‖], and Gorka Basañez[‡3]

From the ‡Unidad de Biofísica, Centro Mixto Centro Superior de Investigaciones Científicas (CSIC)-EuskalHerriko Unibertsitatea/ Universidad del País Vasco (EHU/UPV), Barrio Sarriena s/n, Leioa 48940, Spain, the §Interfaculty Institute of Biochemistry, University of Tübingen, Hoppe-Seyler-Strasse 4, 72076 Tübingen, Germany, and the ¶Max-Planck Institute for Intelligent Systems, Heisenbergstrasse 3, 70569 Stuttgart, Germany, and the ‖German Cancer Research Center, BioQuant, ImNeuenheimer Feld 267, 69120 Heidelberg, Germany

Background: BCL2 family protein interactions with and at mitochondrial membranes are poorly understood.
Results: Fluorescence-based studies applied to minimalist model systems provide new insight into membrane activities of MCL1 and BAK under apoptotic-like conditions.
Conclusion: Membrane interaction modes of MCL1 and BAK share particular features but also display important differences.
Significance: BCL2 family protein function can be modulated at the mitochondrial membrane level through manifold mechanisms.

Proteins belonging to the BCL2 family are key modulators of apoptosis that establish a complex network of interactions among themselves and with other cellular factors to regulate cell fate. It is well established that mitochondrial membranes are the main locus of action of all BCL2 family proteins, but it is difficult to obtain a precise view of how BCL2 family members operate at the native mitochondrial membrane environment during apoptosis. Here, we used minimalist model systems and multiple fluorescence-based techniques to examine selected membrane activities of MCL1 and BAK under apoptotic-like conditions. We show that three distinct apoptosis-related factors (*i.e.* the BCL2 homology 3 ligand cBID, the mitochondrion-specific lipid cardiolipin, and membrane geometrical curvature) all promote membrane association of BCL2-like structural folds belonging to both MCL1 and BAK. However, at the same time, the two proteins exhibited distinguishing features in their membrane association modes under apoptotic-like conditions. In addition, scanning fluorescence cross-correlation spectroscopy and FRET measurements revealed that the BCL2-like structural fold of MCL1, but not that of BAK, forms stable heterodimeric complexes with cBID in a manner adjustable by membrane cardiolipin content and curvature degree. Our results add significantly to a growing body of evidence indicating that the mitochondrial membrane environment plays a complex and active role in the mode of action of BCL2 family proteins.

Apoptotic programmed cell death is a highly conserved and regulated process required for proper development and main- tenance of tissue homeostasis in all metazoans (1). Defects in apoptosis regulation have been linked to many human diseases and are a hallmark of cancer. In vertebrates, most programmed cell death occurs via the intrinsic or mitochondrial apoptotic pathway, wherein a pivotal event is the formation of a protein-permeable pore at the mitochondrial outer membrane (MOM)[4] known as the mitochondrial apoptotic pore (2, 3). Mitochondrial apoptotic pore formation is critically regulated by BCL2 family proteins, which primarily localize to the MOM during apoptosis (1–4).

Members of the BCL2 family can be conveniently classified into three subgroups, based on functional criteria and the conservation of up to four BCL2 homology (BH) motifs (5). The first subgroup corresponds to BCL2-type antiapoptotic proteins, which predominantly act by inhibiting the mitochondrial apoptotic pore and contain either all four BH motifs (BCL2, BCLXL, and BCLW) or BH1–BH3 motifs (MCL1, BFL1, and BCLB). The second subgroup is represented by BAX-type proapoptotic proteins (BAX and BAK), which function as direct effectors of the mitochondrial apoptotic pore and possess BH1–BH3 motifs. A third subgroup corresponds to so-called "BH3-only" proapoptotic proteins (BID, BIM, PUMA, NOXA, BMF, BAD, HRK, and BIK) bearing only a single BH3 motif, which act by triggering BAX/BAK functional activation and thereby also promote mitochondrial apoptotic pore formation.

Despite its utility, the above described classification also has some limitations. First of all, based on sequence and BH motifs alone, it remains unclear what distinguishes BCL2-type proteins from BAX-type proteins (3, 5). Moreover, it has long been

---

[4] The abbreviations used are: MOM, mitochondrial outer membrane; BH, BCL2 homology; MA, membrane-anchoring; PC, phosphatidylcholine; PE, phosphatidylethanolamine; phosphatidylinositol; CL, cardiolipin; Rho, tetramethylrhodamine-5-iodoacetamide; SUV, small unilamellar vesicle(s); LUV, large unilamellar vesicle(s); GUV, giant unilamellar vesicle(s); FCCS, fluorescence cross-correlation spectroscopy; SFCCS, spatial fluorescence cross-correlation spectroscopy; NBD, 7-nitrobenz-2-oxa-1,3-diazole; PDB, Protein Data Bank.

known that under specific circumstances BCL2-type proteins can reverse their antiapoptotic phenotype to transform into BAX-type proapoptotic molecules (5). In addition, it remains debated whether all members within each BCL2 family subgroup share an identical mechanism of action.

From a structural point of view, BCL2-type and BAX-type proteins share a common all-α fold in solution that we will name the BCL2-like structural fold, comprising a primarily hydrophobic core helix surrounded by a bundle of six or seven amphipathic helices and their connecting loops. In addition, most multi-BH motif BCL2 family members contain a C-terminal segment dominated by hydrophobic residues, although they are not generally well conserved sequences. These C-terminal hydrophobic regions normally target multi-BH motif BCL2 family members to mitochondria and anchor them into the MOM; hence, they are regularly termed C-terminal membrane-anchoring (MA) or transmembrane domains (1, 3, 5). Nevertheless, evidence indicates that the C-terminal MA domain is not the sole region determining the targeting and anchoring into the MOM of BCL2 family proteins. As a prominent example, the BH3-only protein BID possessing a BCL2-like structural fold but lacking a C-terminal MA domain efficiently translocates to and inserts into the MOM following apoptotic stimulation, with the mitochondrion-specific lipid CL playing a vital role in this process (6). In addition, it has long been recognized that BCL2-like structural folds of multi-BH motif BCL2 family members contain specific regions that can contribute to targeting and/or anchoring of these proteins into the MOM (7–9, 11–13).

BCL2 family proteins establish an intricate network of interactions among themselves and with many other cellular factors to regulate cell fate. Studies in membrane-free environments revealed a canonical protein-protein interaction mode between pairs of BCL2 family members (1). Here, an elongated hydrophobic groove present in BCL2-like structural folds of BCL2-type and BAX-type proteins encompassing their BH1–BH3 motifs acts as the "acceptor site" for binding a "ligand" helix of a proapoptotic BCL2 family partner comprising its BH3 motif (1). Nevertheless, increasing evidence indicates that BCL2 family proteins can exhibit different interaction modes at the cytoplasm and at the MOM level (4). In addition, recent studies showed that many BCL2 family members are in a dynamic equilibrium between the cytosol and the MOM that depends upon the physiological status of the cell. Under non-apoptotic conditions, BAX, BAK, BCLXL, and MCL1 are constantly retro-translocating from mitochondria into the cytosol; in response to apoptotic stress, retrotranslocation is stopped while all of these proteins accumulate at the MOM (13–17). How BCL2 family proteins retrotranslocate under non-apoptotic conditions is increasingly understood (14–18), but the mechanisms leading to general BCL2 family protein accumulation at the MOM following a death stimulus are poorly understood. On top of this, it is also recognized that the mode of action of BCL2 family proteins can be modulated by compositional and structural features of the lipid bilayer portion of the MOM. However, we are only beginning to understand the precise influence of the MOM lipid bilayer environment on the mechanism of action of particular BCL2 family proteins (4, 19–23).

Studying individual BCL2 family members or their mutual relationship at mitochondria in the course of apoptosis is a challenge because of the complex compositional nature of the MOM, which is further complicated by the fact that it can be spatially and dynamically connected to the mitochondrial inner membrane and to the endoplasmic reticulum, depending on the physiological status of the cell (22). During the last 2 decades, simple model systems that bypass cellular complexity and compositional diversity have provided powerful experimental means to obtain mechanistic insights into the apoptosis-regulatory mode of action of BCL2 family proteins (2, 6, 19–27).

Here, we used minimalist model systems and a variety of fluorescence-based techniques to examine, side-by-side, membrane association and membrane level heterodimerization activities of BCL2-like structural folds belonging to MCL1 and BAK. Our results indicate that different apoptosis-related factors promote membrane binding of both proteins via mechanisms displaying common and distinguishing features. In addition, SFCCS and FRET analyses revealed that the BCL2-like structural fold of MCL1 forms a stable heterodimeric complex with cBID at the membrane level, whereas that of BAK does not. Furthermore, we report that MCL1·cBID heterodimerization is adjustable by membrane CL content and geometrical curvature. Altogether, our results support the notion that the function of BCL2 family members can be modulated at the mitochondrial membrane level through manifold mechanisms.

Experimental Procedures

Materials—Egg phosphatidylcholine (PC) and phosphatidylethanolamine (PE), brain phosphatidylinositol (PI), bovine heart cardiolipin (CL), 1,2-diphytanoyl-*sn*-glycero-3-phosphoethanolamine-*N*-(7-nitro-2–1,3benzoxadiazol-4-yl), and L-α-phosphatidylethanolamine-*N*-(lissaminerhodamine B sulfonyl) were purchased from Avanti Polar Lipids, Inc. (Alabaster, AL). DiIC18, Alexa Fluor 488-maleimide, Alexa Fluor 647-maleimide, [*N*,*N*′-dimethyl-*N*-(iodoacetyl)-*N*′-(7-nitrobenz-2-oxa-1,3-diazolyl)ethylenediamine, and tetramethylrhodamine-5-iodoacetamide (Rho)-maleimide were purchased from Molecular Probes, Inc. (Eugene, OR). KCl, HEPES, EDTA, sucrose, sodium carbonate, Rho-10-kDa dextran, and fatty acid free BSA were purchased from Sigma-Aldrich (Cambridge, UK). LabTec chambers were purchased from NUNC (Munich, Germany).

Recombinant Proteins—All proteins were purified from soluble fractions of bacterial extracts obtained in the absence of detergents and were >95% pure as evaluated by Coomassie-stained SDS-PAGE. Recombinant mouse MCL1 lacking the N-terminal 151 amino acids and the C-terminal 23 amino acids (MCL1ΔN151ΔC23) and its S177C and R244E mutants, recombinant human BAK lacking the carboxyl-terminal 21 amino acids (BAKΔC21) and its C166S and R127E mutants, and recombinant caspase-8-cleaved mouse BID (cBID) and its C30S or C30S/D95A mutants were all expressed and purified as described previously (20, 21). Mutations were carried out by site-directed mutagenesis using the following primers: MCL1 S177C, 5′-GCTCCAAGGACTGCAAGCCTCTGGGCGA-3′ (forward) and 5′-TCGCCCAGAGGCTTGCAGTCCTTG-

GAGC-3′ (reverse); BID C30S, 5′-CTCCAAAGCTCTG-GCAGTACTCGCCAAGAGC-3′ (forward) and 5′-GCTCT-TGGCGAGTACTGCCAGAGCTTTGGAG-3′ (reverse). The cBID D95A, BAK C166S, BAK R127E, and MCL1 R244E plasmids were purchased from TopGenetech (Ontario, Canada). Monocysteine proteins were conjugated with Alexa fluorescent dyes as follows: (i) MCL1ΔN151ΔC23^{S177C}, with the Cys mutation localized at the loop between α1 and α2, was labeled with the green (g) fluorophore Alexa488, thereby generating MCL1ΔN151ΔC23$^{S177C-Alexa488}$ variant, which is named MCL1$_g$ hereafter; (ii) BAKΔC21^{C166S,C14} was also labeled with Alexa488 in endogenous C14 localized at the N-terminal loop, thereby generating the BAKΔC21$^{C166S,C14-Alexa488}$ variant named BAK$_g$ hereafter; and (iii) cBID^{C30S,C126} was labeled with the red (r) fluorophore Alexa647 in endogenous Cys126 localized at the N terminus of α5 to generate cBID$^{C30S,C126-Alexa647}$ variant named cBID$_r$ hereafter (Fig. 1*A*). On the other hand, for FRET experiments, MCL1ΔN151ΔC23^{S177C} and BAKΔC21^{C166S,C14} were labeled with NBD to generate variants that are named NBD-MCL1 and NBD-BAK, respectively, hereafter, whereas cBID^{C30S,C126} was labeled with Rho to generate a variant named Rho-cBID hereafter.

Protein Tryptophan (Trp) Fluorescence Measurements—Protein tryptophan fluorescence spectroscopy experiments were performed in an 8100 Aminco-Bowman luminescence spectrometer equipped with double-grating excitation and single-grating emission monochromators (JobinYvon, Edison, NJ). The measurements were taken in 4 × 4-mm quartz cuvettes. Trp fluorescence spectra were recorded by averaging 3–5 scans over a 300–400 nm range at a scan rate of 1 nm/s, using an excitation wavelength of 295 nm. The slit widths for excitation and emission were kept at 4 nm. The contribution of buffer to sample fluorescence was subtracted as blank. Protein concentration was 300 nM.

Liposome Preparation—Lipid mixtures were first co-dissolved in chloroform/methanol (2:1), and organic solvent was removed by evaporation under a nitrogen stream followed by incubation under vacuum for 2 h. Dry lipid films were resuspended in 100 mM KCl, 10 mM Hepes, pH 7.0, and 0.1 mM EDTA (KHE buffer). Multilamellar vesicles were either (i) subjected to sonication to obtain small unilamellar vesicles (SUV) or (ii) subjected to 10 freeze/thaw cycles and subsequently extruded 10 times through two polycarbonate membranes of 0.1-μm pore size to obtain large unilamellar vesicles (LUV). In SUV/LUV-type liposomes, we used 55:35:10 PC/PE/PI (mol/mol/mol) (0% CL) as a "template" lipid composition in which increasing proportions of PC were substituted by CL to yield the following liposome compositions: 51:35:10:4 PC/PE/PI/CL (mol/mol/mol/mol) (4% CL), 40:35:10:15 PC/PE/PI/CL (mol/mol/mol/mol) (15% CL), 25:35:10:30 PC/PE/PI/CL (mol/mol/mol/mol) (30% CL), and CL (100% CL). GUV-type vesicles were prepared as described previously (27). Briefly, around 4 μl of the lipid mixture stock (1 mM) in chloroform was spread on the platinum wires of the electroformation chamber. After solvent evaporation, the wires were immersed in 200 mM sucrose buffer, and electric pulses of 10 Hz were provided for 2 h, followed by 2-Hz pulses for 30 min. Due to lower GUV stability relative to LUV/SUV-type

liposomes, we used GUV with the following lipid compositions: PC (0% CL), 96:4 PC/CL (mol/mol) (4% CL), 85:15 PC/CL (mol/mol) (15% CL), 70:30 PC/CL (mol/mol) (30% CL), and CL (100% CL).

Quasielastic Light Scattering Measurements—Quasielastic light scattering measurements were performed in a Malvern Zeta Sizer Nano ZS (Malvern Instruments, Malvern, UK). To analyze liposome size distribution, a helium-neon laser beam of 5 milliwatts was used, and the light scattered by the sample (λ = 633 nm) was detected with a photomultiplier placed perpendicular to the beam. Liposome size distribution was estimated based on particle mass (% volume) rather than scattering (% intensity).

GUV Permeabilization Experiments—BCL2 family proteins and Rho-10-kDa dextran were mixed in LabTec chambers (NUNC) with KHE, and 80 μl of 1,2-diphytanoyl-*sn*-glycero-3-phosphoethanolamine-*N*-(7-nitro-2-1,3-benzoxadiazol-4-yl)-labeled GUV composed of 70:30 PC/CL were then added to a final volume of 400 μl. After 2 h of incubation at room temperature, images were collected with a confocal fluorescence microscope (see microscope specifications below). The percentage of internalization of Rho-10-kDa dextran to the lumen of GUV was measured with ImageJ software as described previously (27). Protein concentrations were 300 nM for BAK$_g$/BAK, 400 nM for MCL1$_g$/MCL1, and 15 nM for cBID$_r$/cBID.

Cytochrome c Release Assay—Mouse embryonic fibroblasts were kindly provided by Dr. Isabel Marzo (Universidad de Zaragoza, Zaragoza, Spain). Mouse embryonic fibroblasts were homogenized with the vertical passing of three rounds of 20, 15, and 10 strokes in a precooled 5-ml glass-Teflon Potter-Elvehjem homogenizer. Mitochondria-enriched fraction was obtained by differential centrifugation of the sample, using the following mitochondrial isolation buffer (MIB): 210 mM mannitol, 70 mM sucrose, 10 mM Hepes (pH 7.5), 1 mM EDTA, and protease inhibitors. Mitochondria were kept on ice and used within 2 h of preparation. Isolated mitochondria (1 mg protein/ml) were incubated with cBID/cBID$_r$ (5 nM) alone or together with MCL1/MCL1$_g$ (200 nM) for 30 min at 30 °C in 125 mM KCl, 5 mM KH$_2$PO$_4$, 2 mM MgCl$_2$, 1 mM DTT, and 10 mM HEPES-KOH, pH 7.2 (V_{final} = 50 μl). Subsequently, reaction mixtures were centrifuged at 14,000 × *g* for 10 min, and supernatant and pellet fractions were subjected to 15% SDS-PAGE and immunoblotting using anti-cytochrome *c* 7H8.2C-12 antibody.

Equilibrium Sucrose Gradient Centrifugation of Liposome/Protein Mixtures—Proteins (250 nM) were first co-incubated with or without SUV/LUV (250 μM) in KHE buffer for 30 min at 25 °C. In the alkali extractability experiments, protein-liposome mixtures were then incubated in 100 mM Na$_2$CO$_3$ (pH 11.5) for 30 min on ice. Samples were then adjusted to 1.4 M sucrose and loaded at the bottom of a discontinuous sucrose gradient containing a medium layer of 0.8 M sucrose and an upper layer of 0.5 M sucrose. Next, samples were centrifuged at 100,000 rpm for 3 h in a Beckman Optima TLX Benchtop ultracentrifuge using a TLA 120.2 rotor, followed by collection of four 250-μl fractions. Samples were subsequently subjected to reducing SDS-PAGE on 15% gels, followed by on-gel fluorescence visualization using a Molecular Imager Versadoc (Bio-Rad). To identify liposome-containing fractions of the gradient,

liposomes were prepared with 0.5 mol % L-α-phosphatidylethanolamine-N-(lissaminerhodamine B sulfonyl). In all cases, at least 85% of L-α-phosphatidylethanolamine-N-(lissaminerhodamine B sulfonyl) fluorescence was found at the uppermost two fractions of the gradient. Thus, we considered that the top two fractions correspond to the liposome-containing fractions of the gradient, whereas the bottom two fractions correspond to the liposome-free fractions of the gradient.

Confocal Microscopy Fluorescence Cross-correlation Spectroscopy (FCCS) Analysis—For microscopy observations of protein recruitment to GUV, fluorescently labeled proteins and liposomes were incubated together for 2 h at 22 °C in an observation chamber previously blocked with BSA to prevent attractive interactions between the vesicles and the glass substrate. Images were recorded in an inverted confocal fluorescence microscope (Nikon DECLIPSE C1, Nikon Inc., Melville, NY) with a total internal reflection fluorescence ×60 oil immersion objective. The excitation wavelengths used were 488, 561, and 635 nm, and emitted fluorescence was recorded using band pass filters of BP515, BP593, and a long pass filter of LP650, respectively. Fluorescence images were processed with ImageJ software using the plug-in "Radial profile," measuring integrated intensities along concentric circles centered at the middle of the GUV. Next, the measured intensity corresponding to the protein bound to the GUV membrane was normalized to the values obtained in solution.

FCCS measurements were performed at 22 °C using a ConfoCor 3 module with attenuated excitation light from argon ion (488 nm) and helium-neon lasers (633 nm), and emitted fluorescence was recorded using a band pass filter of BP530 and a long pass filter of LP655, respectively. For solution FCCS experiments, we first calibrated the size of the focal volume using free Alexa488 and Alexa633 dyes. MCL1$_g$ and cBID$_r$ were incubated in the observation chamber for 1 h before carrying out FCCS measurements. To obtain auto- and cross-correlation curves, raw fluorescence fluctuation data were fitted to a three-dimensional diffusion model with homemade software. For two-focus SFCCS measurements in GUV, photon arrival times were recorded with a Flex 02-01D/C hardware correlator, and the data were also analyzed with homemade software. Here, once the microscope had been aligned, the detection volume was repeatedly scanned perpendicular across the GUV equator in two parallel lines (the distance between the two lines, d, was measured by photobleaching on a film of dried fluorophores). From these two traces, the focal volume can be determined, avoiding the need for calibration. The measurement time was 300 s, and the bin time was 2 μs. Fluorescence intensity data were arranged as a matrix such that every row corresponded to one line scan. The rows were aligned to correct for membrane movements by calculating the maximum of a running average over several hundred line scans and shifting it to the same column. The autocorrelation and spectral and spatial cross-correlation curves were computed from the intensity traces, and irregular curves resulting from instability and distortion were excluded from the analysis. We fitted the auto- and cross-correlation functions with a nonlinear least-squares global fitting algorithm (2Dimensions 2Focus 2Color). As a result of the analysis of FCCS data, surface concentrations of single color particles (C_r and C_g) and two-color particles (CC_{rg}) as well as their diffusion coefficients were determined. FCCS results were also corrected for fluorescence cross-talk and for protein labeling degrees (90% for MCL1$_g$, 80% BAK$_g$, 70% for cBID$_r$, and 100% for cBID$_r$ D95A). Complex % values were calculated with respect to the amount of the green particles ($CC_{rg} \times 100/C_g$), being the percentage value between CC_{rg} two-color particles (the green and red complexed molecules) and the total green particles (the free and the complexed ones).

FRET Measurements—FRET experiments were performed in an 8100 Aminco-Bowman luminescence spectrometer. Briefly, 100 nM NBD-MCL1/BAK (donor) and 400 nM Rho-cBID (acceptor) were incubated with and without liposomes (200 μM lipid) for 30 min at room temperature in the dark. Fluorescence spectra were recorded by averaging 3–6 scans over a 510–620 nm range at a scan rate of 1 nm/s, using an excitation wavelength of 465 nm for NBD. The slit widths for excitation and emission were 8 and 4 nm, respectively. We prepared four samples: B (blank, without donor or acceptor dyes), D (donor-containing), A (acceptor-containing), and DA (donor- and acceptor-containing). Subtraction of the B signal from that of D corrects for the significant light scattering signal and yields the net donor spectrum, whereas subtraction of the A signal from that of DA corrects for both scattering and any signal due to direct excitation of the acceptor, thereby yielding the net donor + acceptor spectrum. FRET signals were estimated as described previously (28), by calculating ratios of net R_{D+A} (*i.e.* ratio of fluorescence of net donor + acceptor spectrum signal at 580 nm and of fluorescence of donor + acceptor spectrum signal at 540 nm) and net R_D (*i.e.* ratio of fluorescence of net donor spectrum signal at 580 nm and of fluorescence of net donor spectrum signal at 540 nm).

Results

Design of Experimental Systems—Recombinant monocysteine versions of BCL2-like structural folds belonging to MCL1, BAK, and the apoptogenic form of BID (cBID) were site-specifically labeled with the green (g) Alexa488 fluorophore or the red (r) Alexa647 fluorophore to generate fluorescent MCL1$_g$, BAK$_g$, and cBID$_r$ variants, respectively (Fig. 1A). We examined whether the mutagenesis and/or labeling procedures altered protein global structure or functionality. As shown in Fig. 1B, intrinsic fluorescence spectra of MCL1$_g$, BAK$_g$, and cBID$_r$ were virtually indistinguishable from those of native protein counterparts. The three fluorescently labeled variants also retained the ability of their parent unlabeled proteins to modulate membrane permeability, as revealed by an assay measuring internalization of Rho-10-kDa dextrans into 30% CL GUV (Fig. 1C). In addition, we examined the ability of fluorescently labeled MCL1 and cBID variants to regulate mitochondrial cytochrome c release. As shown in Fig. 1D, cBID$_r$ released cytochrome c as effectively as cBID, whereas MCL1$_g$ abolished this process akin to MCL1. Altogether, this set of experiments demonstrates that our fluorescently labeled BCL2 variants preserve basic structural and functional properties of their native protein counterparts.

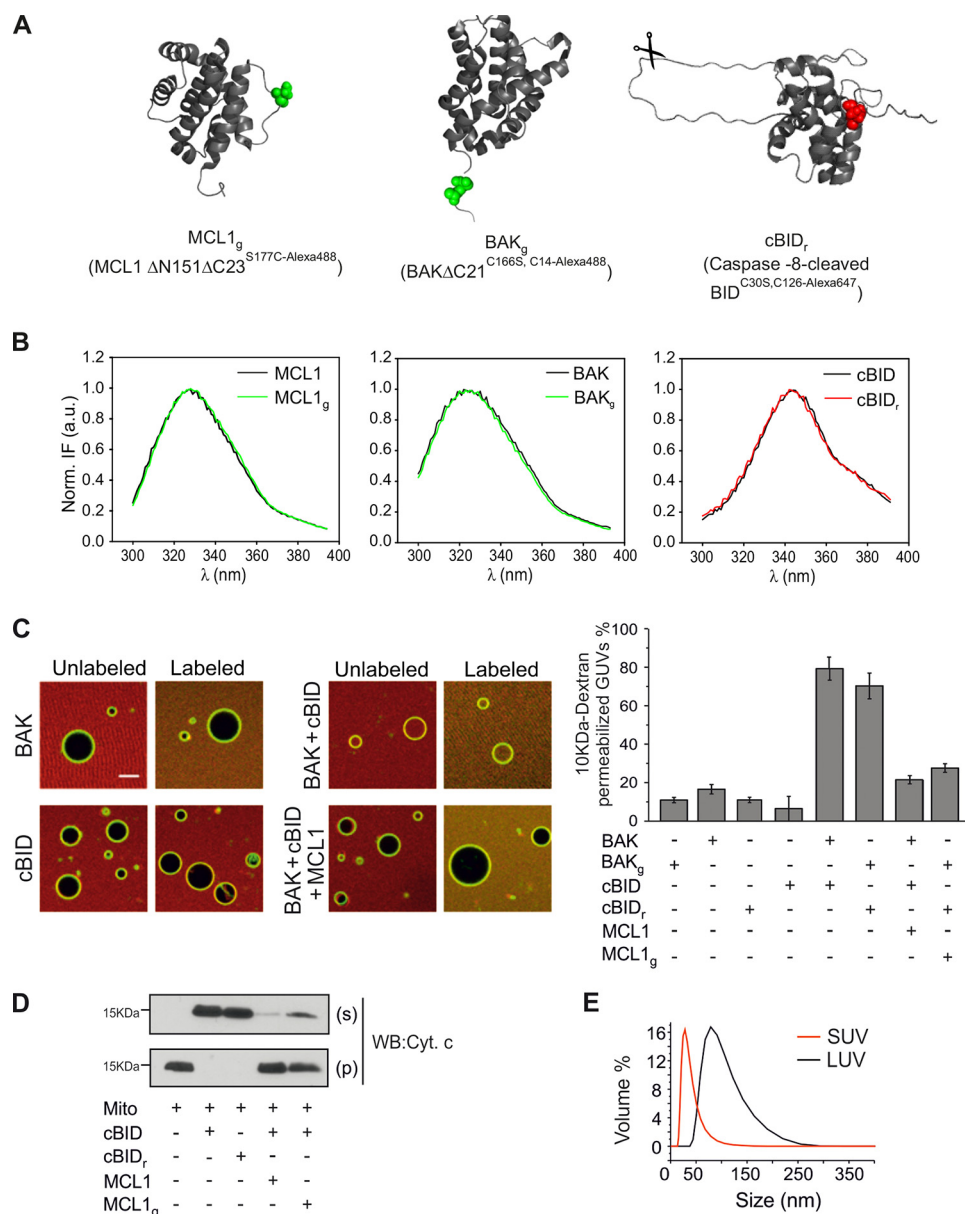# Comparison of Membrane Interaction Modes of MCL1 and BAK

FIGURE 1. **MCL1$_g$, BAK$_g$, and cBID$_r$ maintain structural and functional properties of native unlabeled counterparts.** *A*, three-dimensional structures of MCL1ΔN151ΔC23 (PDB code 1WSX), BAKΔC21 (PDB code 2IMS), and BID (PDB code 1DDB) displaying as *colored spheres* the monocysteine residue where the Alexa-fluorophore is conjugated to generate MCL1$_g$, BAK$_g$, and cBID$_r$, variants used in this study. *Scissors*, caspase-8 cleavage site (Asp^{59} ↓ Gly^{60}) in the cBID structure. *B*, Trp fluorescence spectra of MCL1$_g$, BAK$_g$, and cBID$_r$ variants and their wild-type, unlabeled counterparts ($n = 3$). *C*, percentage of Rho-10-kDa dextran-permeabilized GUV in the presence or absence of the indicated BCL2 proteins. Mean values ± S.D. (*error bars*) correspond to two independent experiments. *D*, effect of BCL2 proteins on the release of cytochrome *c* from mitochondria isolated from mouse embryonic fibroblasts. *E*, liposome size distribution analyzed by quasielastic light scattering for 30% CL SUV (*red trace*) and 30% CL LUV (*black trace*). *IF*, intensity of fluorescence; *a.u.*, arbitrary units; *WB*, Western blot.

As model membrane systems for our mechanistic studies, we used liposomes of variable sizes (SUV, LUV, and GUV) containing different molar percentages of CL (0% CL, 4% CL, 14% CL, 30% CL, and 100% CL). Due to their small size and high geometrical curvature (Fig. 1*E*), we consider SUV-type liposomes morphological surrogates of MOM-mitochondrial inner membrane contact sites (CS) and other curved lipid surfaces thought to be present at specialized regions of the MOM, such as mitochondrial membrane fission sites and MOM-endoplasmic reticulum junctions. Of note, evidence indicates that the number of MOM-mitochondrial inner membrane CS, mitochondrial membrane fission sites, and MOM-endoplasmic reticu-

lum junctions increases during apoptosis (29–31). By contrast, LUV-type and GUV-type liposomes display negligible membrane curvature at the protein scale due to their large size, thereby emulating the flat lipid surface thought to predominate at the MOM under non-apoptotic conditions. Regarding the lipid compositions chosen, we consider that (i) 0–4% CL represents the average CL content of the MOM under normal conditions, (ii) 14–30% CL reflects the CL content present at mitochondrial CS, and (iii) 100% CL emulates CL microdomains that may be formed during the apoptotic process at localized areas of the MOM (32). The latter are not unprecedented, because CL microdomains have been described in bacterial

membranes (33). Of note, although the role of CL during apoptosis is still unsettled, recent reports indicate that CL and/or its derivatives accumulate at the MOM early in the course of apoptotic cell death (34, 35). It should also be taken into account that the BCL2-like structural folds of MCL1, BAK, and cBID are primarily oriented toward the cytosol-facing leaflet of the MOM, which should be enriched in CL relative to the inter-membrane-facing leaflet of the MOM in accord with the asymmetrical interleaflet distribution of negatively charged lipids commonly found in biomembranes (32).

cBID, CL, and Curvature Promote Membrane Association of MCL1$_g$—In a first set of experiments, we evaluated whether MCL1$_g$·membrane binding is affected by three different apoptosis-related factors: (i) the MCL1 ligand cBID, (ii) the mitochondria lipid trademark CL, and (iii) membrane geometrical curvature. To this aim, we incubated liposomes of variable sizes (SUV, LUV, and GUV) and CL contents with MCL1$_g$ alone, cBID$_r$ alone, or MCL1$_g$ plus cBID$_r$.

To begin with, SUV-type or LUV-type liposomes were used as model membrane systems. After incubating the protein(s) with the vesicles, liposome-containing and liposome-free fractions were separated by equilibrium sucrose gradient ultracentrifugation, and the protein contents of each fraction were quantified by SDS-PAGE and fluorescence intensity analysis. On the one hand, in the absence of cBID$_r$, we found minimal amounts of MCL1$_g$ bound to MOM-like SUV or LUV containing 0–4% CL (Fig. 2, *A* and *B*). In contrast, appreciable amounts of MCL1$_g$ alone bound to mitochondrial CS-like SUV or LUV containing 14–30% CL, whereas virtually all MCL1$_g$ associated by itself with pure CL SUV or LUV (Fig. 2, *A* and *B*) (data not shown). Of note, much more MCL1$_g$ bound on its own to SUV containing 14–30% CL than to LUV containing 14–30% CL (Fig. 2, *A* and *B*). Thus, high membrane geometrical curvature directly promotes MCL1$_g$ association with liposomes containing CL levels present at mitochondrial CS. On the other hand, the addition of cBID$_r$ further stimulated MCL1$_g$ binding to mitochondrial CS-like SUV and LUV (Fig. 2, *A* and *B*). cBID$_r$ also enhanced MCL1$_g$ binding to MOM-like SUV but not to MOM-like LUV. Of note, the capacity of cBID$_r$ to stimulate MCL1$_g$ binding to the liposomes correlated with the ability displayed by cBID$_r$ alone for binding to the vesicles.

We next analyzed MCL1$_g$ binding to GUV-type liposomes containing increasing CL contents in the absence or presence of cBID$_r$. Here, vesicles were incubated with the protein(s), and then the fluorescence intensity increase at the rim of the GUV membrane of multiple individual vesicles was visualized by confocal fluorescence microscopy and quantified. In qualitative agreement with results obtained with low curvature LUV-type liposomes, MCL1$_g$ by itself only bound successfully to pure CL GUV. Furthermore, cBID$_r$ enhanced MCL1$_g$ binding to mitochondrial CS-like GUV but not to MOM-like GUV, correlating with the intrinsic capacity of cBID$_r$ for binding the former but not the latter type of liposome, which also agrees with the behavior displayed by these proteins in the low curvature LUV system (Fig. 2, *B–D*). In summary, this set of results demonstrates that three distinct apoptosis-related factors (cBID, CL, and curvature) promote membrane association of the BCL2-like structural fold of MCL1.

Different Membrane Association Modes of MCL1$_g$ Revealed by Mutagenesis and Alkali Extractability—Solution-based binding studies revealed a canonical protein-protein interaction mode between BH3-only proteins and BCL2-type or BAX-type proteins based on engagement of the BH3 domain of the proapoptotic ligand into an elongated hydrophobic groove present at the surface of the BCL2-type or BAX-type receptor (1, 3). However, it is currently debated whether this canonical BH3-into-groove interaction mechanism is the exclusive mediator of functional interactions between different BCL2 family members at the MOM environment (4). To gain more insight into how cBID$_r$ stimulates MCL1$_g$ membrane association in our reconstituted minimalist system, we evaluated the impact of cBIDD95A and MCL1 R244E point mutations that disrupt a critical intermolecular salt bridge according to the canonical BH3-into-groove interaction mechanism (1) (Fig. 3*A*).

Selective disruption of this protein-protein interaction mode through mutagenesis abolished cBID-mediated stimulation of MCL1 binding to 0% CL SUV (Fig. 3*B*), 30% CL LUV (Fig. 3*C*), and 30% CL GUV (Fig. 3*D*). By contrast, the cBID D95A and MCL1 R244E point mutations had minimal impact on MCL1 binding to 30% CL SUV (Fig. 3*B*), 100% CL LUV (Fig. 3*C*), and 100% CL GUV (Fig. 3*D*). These results together with those described in Fig. 2 indicate that MCL1$_g$ can associate with liposomal membranes in two broadly distinct manners: (i) by engaging to membrane-bound cBID through the same canonical BH3-into-groove interaction mechanism described in solution binding studies or (ii) by directly binding to the liposomal lipid bilayer in a manner that depends on its CL content and geometrical curvature.

We also wished to discriminate whether MCL1$_g$ is loosely bound to or firmly embedded into the liposomal membrane under different conditions. To this aim, we analyzed the alkali extractability of MCL1$_g$ from SUV or LUV containing different amounts of CL in the presence or absence of cBID$_r$ (Fig. 3*E*). Upon alkali treatment, the majority of MCL1$_g$ was extracted from mitochondrial CS-like LUV, whereas a substantially lower fraction of MCL1 was extracted from mitochondrial CS-like SUV, and minimal MCL1$_g$ was extracted from pure CL vesicles (Fig. 3*E*). In all cases, cBID$_r$ had little effect in MCL1$_g$ membrane extractability. These data suggest that CL and curvature, but not cBID, promote membrane insertion of MCL1$_g$.

MCL1$_g$ and cBID$_r$ Form Stable Heterodimeric Complexes in CS-like GUV but Not in Pure CL GUV—We next wished to analyze the ability of MCL1 to heterodimerize with cBID in solution and in the context of an intact lipid bilayer membrane environment. To this aim, we used FCCS and its variant SFFCS (36), which allowed us to obtain quantitative information of diffusion coefficients (*D*), concentrations, and complex formation between two spectrally different labeled species from the analysis of their autocorrelation and cross-correlation curves.

In a membrane-free environment, a fairly small cross-correlation curve for the MCL1$_g$·cBID$_r$ complex was observed (Fig. 4*A*, *blue line*), with a low percentage of complex formation (~7%) estimated at the highest protein concentrations tested (Fig. 4*C*). Nevertheless, when MCL1$_g$ was incubated with the cBID$_r^{D95A}$ mutant under the same conditions, the extent of cross-correlation decreased to background levels, suggesting
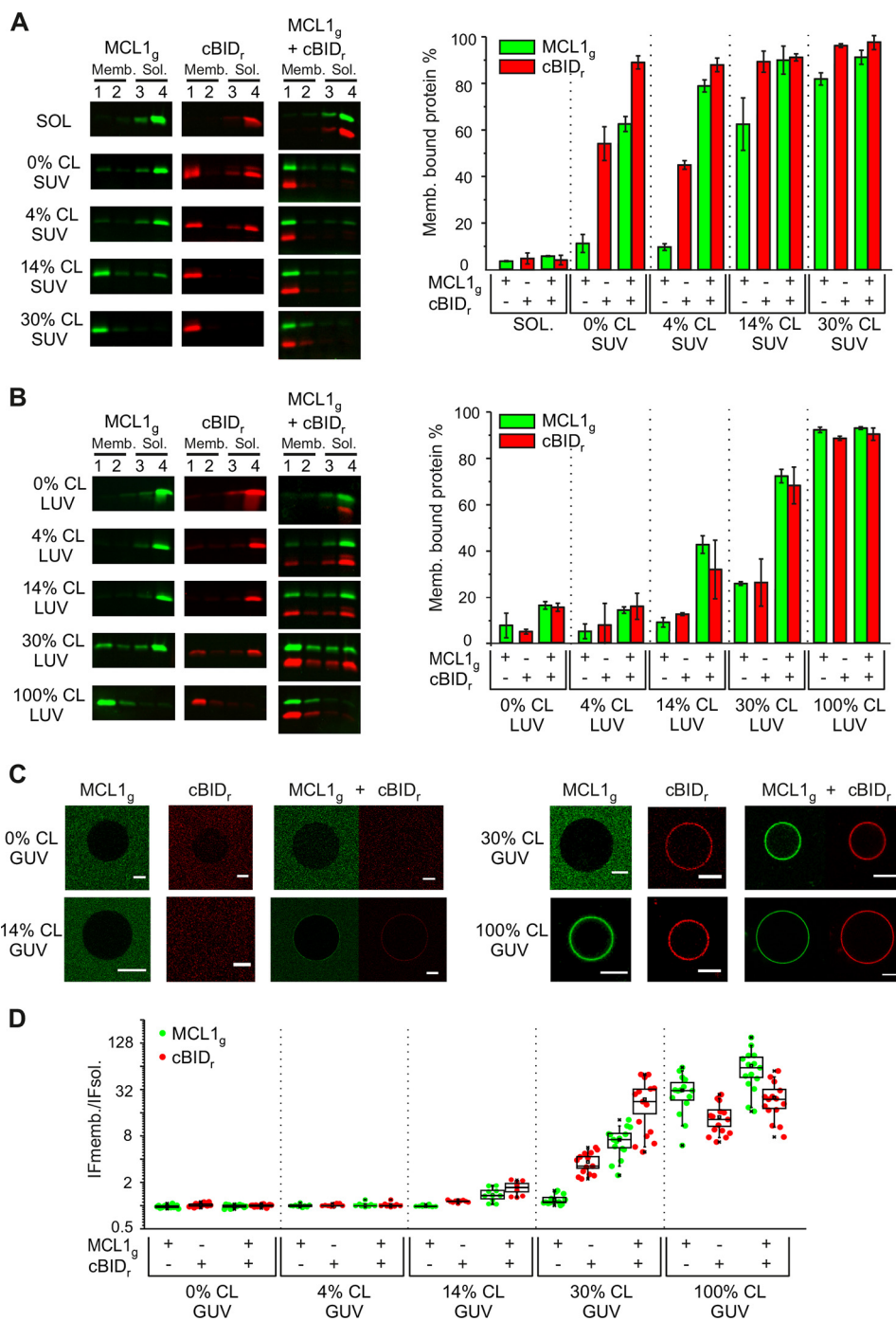
FIGURE 2. **cBID$_r$, CL, and curvature promote MCL1$_g$ binding to liposomal membranes.** *A* and *B*, SUV and LUV recruitment assay. *Left-hand panels*, Proteins were incubated for 30 min in the absence (*SOL*) or presence of SUV- or LUV-type liposomes containing different amounts of CL, followed by sucrose-gradient centrifugation to separate membrane-free fractions (*Sol.*) and membrane-containing fractions (*Memb.*) and analysis by SDS-PAGE and fluorescence detection for MCL1$_g$ (*green*) and cBID$_r$ (*red*) bands. *Right-hand panels*, quantitation of binding of indicated proteins to SUV- or LUV-type liposomes containing different amounts of CL. Protein and lipid concentrations were 250 nM and 250 μM, respectively. Data correspond to mean values $\pm$ S.D. (*error bars*) for at least two independent experiments. *C* and *D*, GUV recruitment assay. *C*, indicated proteins were incubated with GUV containing different amounts of CL followed by analysis of samples by confocal fluorescence microscopy. *Scale bar*, 10 μm. *D*, from the confocal fluorescence images, the ratio of maximum normalized integrated intensity values in membrane (*IFmemb.*) and solution (*IFsol.*) fluorescence obtained from radial profiles was measured for MCL1$_g$ (100 nM) and cBID$_r$ (20 nM) in GUV of the indicated lipid compositions. In this box chart and raw data (*dots*) representation, the *box* represents the 96% confidence interval; *inside* the *box*, the media and median are represented by the *small square* and the *line*, respectively; and the errors correspond to 80% of the data. For each condition, at least 10 GUV were analyzed from 2–3 independent experiments.

that the weak MCL1$_g$·cBID$_r$ complex formation occurred through a canonical BH3-into-groove interaction mechanism (Fig. 4).

Next, we evaluated MCL1$_g$·cBID$_r$ heterodimerization at the level of the GUV membrane by SFCCS. To this aim, we first used mitochondrial CS-like GUV containing 30% CL, because we have previously shown that cBID$_r$ strongly stimulates MCL1$_g$ binding to this type of liposome (Fig. 2D). Indeed, the good quality of MCL1$_g$ and cBID$_r$ autocorrelation curves obtained in 30% CL GUV confirmed that MCL1$_g$ and cBID$_r$
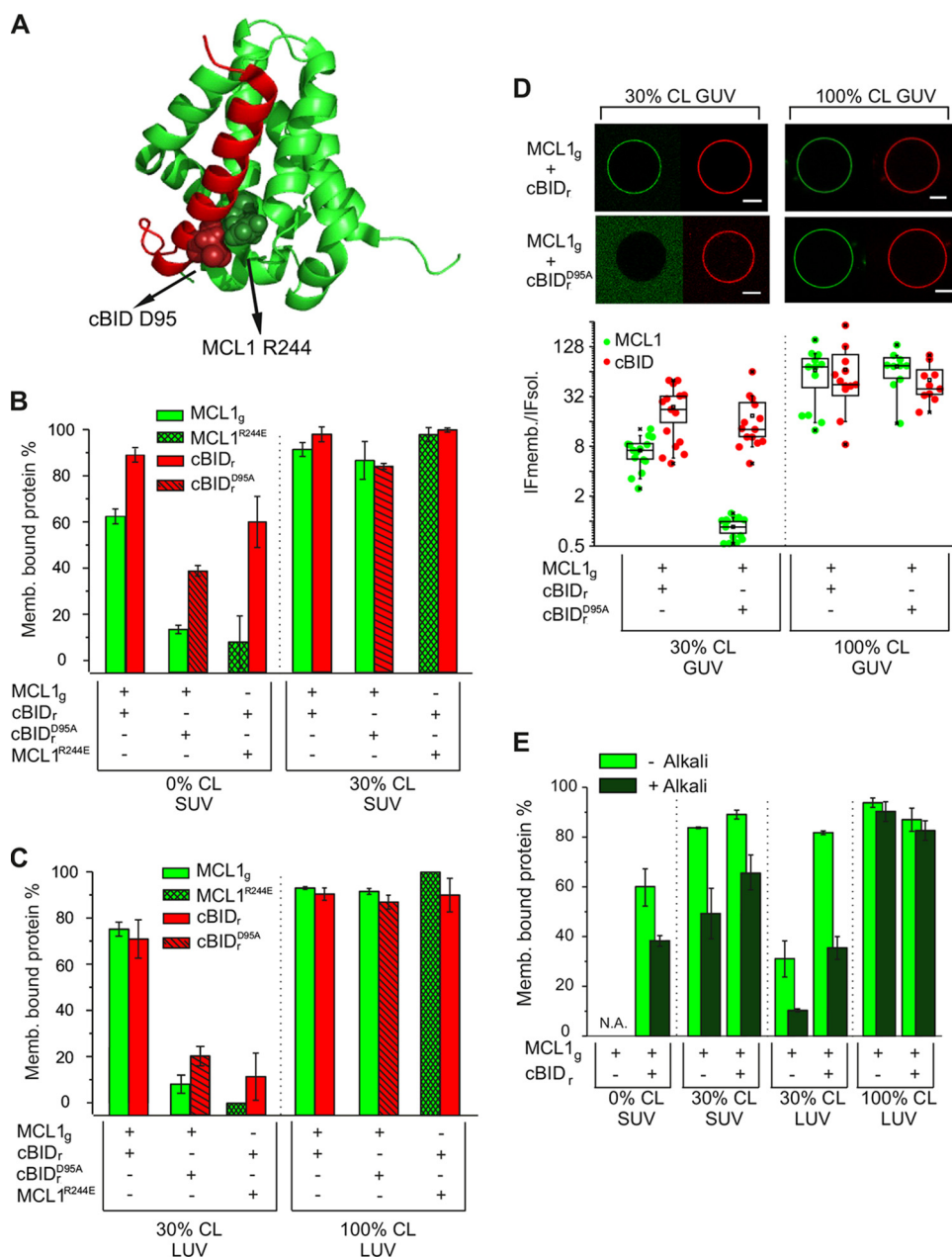
FIGURE 3. **Different membrane association modes of MCL1$_g$.** *A*, structural representation of BID BH3 domain (*red*) bound to MCL1ΔN151ΔC23 (*green*), highlighting as *spheres* BID Asp^{95} and MCL1 Arg^{244} residues implicated in BID BH3-MCL1 groove interaction (PDB code 2KBW). *B* and *C*, effect of MCL1^{R244E} and cBID$_r^{D95A}$ mutations on protein binding to SUV-type or LUV-type vesicles containing different amounts of CL. cBID$_r^{D95A}$ recruitment to liposomes was assessed as described in the legend to Fig. 2, *A* and *B*, whereas MCL1^{R244E} recruitment was assessed by immunoblotting and densitometric quantitation. *D*, effect of cBID$_r^{D95A}$ on MCL1$_g$ recruitment to GUV. MCL1$_g$ and cBID$_r$/cBID$_r^{D95A}$ concentrations were 100 and 5 nM, respectively (30% CL GUV assays) and 2 and 1 nM, respectively (100% CL GUV assays). Other conditions were as described in the legend to Fig. 2. *E*, alkali extractability assay. Proteins preincubated with liposomes were treated with (+*Alkali*) or without (−*Alkali*) 100 mM Na$_2$CO$_3$, pH 11.5, and protein partition was assessed as described in Fig. 2. *Error bars*, S.E.

efficiently localize to the membrane of these vesicles (Fig. 5*A*, *left*, *green* and *red lines*). Importantly, SFCCS analysis showed that MCL1$_g$ and cBID$_r$ form stable complexes at the membrane of 30% CL GUV, reflected by the large positive amplitude of the cross-correlation curve (Fig. 5*A*, *left*, *blue line*). To try estimating the binding affinity between the two proteins at the membrane of these GUV, we analyzed MCL1$_g$·cBID$_r$ complex formation at a wide range of MCL1$_g$ and cBID$_r$ concentrations (Fig. 5*A*, three-dimensional plot at the *right*). Elevated values of complex formation were obtained at all protein concentrations,

indicating that the affinity between membrane-localized MCL1$_g$ and cBID$_r$ in CS-like GUV is so high that MCL1$_g$·cBID$_r$ complex formation is always saturated. We also sought to determine whether MCL1$_g$·cBID$_r$ complex formation in this type of liposome is reversible. To this aim, we added an excess of unlabeled cBID to 30% CL GUV that had been previously co-incubated with MCL1$_g$ and cBID$_r$ (Fig. 5*B*). Adding an excess of unlabeled cBID drastically decreased the amplitude of the MCL1$_g$·cBID$_r$ cross-correlation curve and diminished the percentage of MCL1$_g$·cBID$_r$ complex forma-
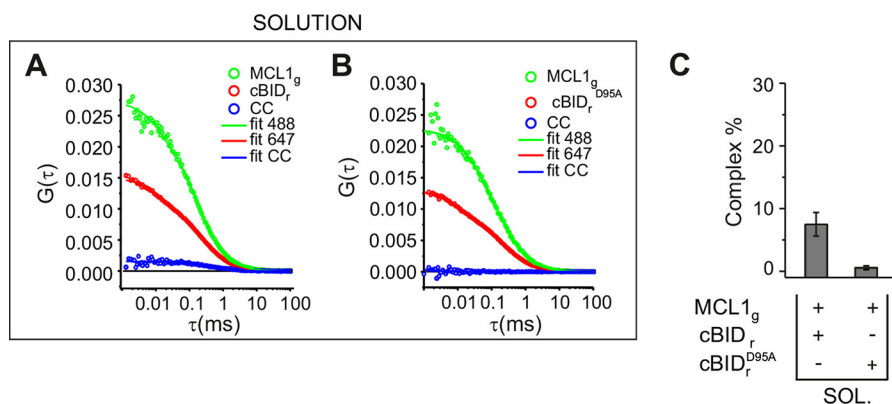
SOLUTION

FIGURE 4. **FCCS analysis indicates weak MCL1$_g$·cBID$_r$ heterodimerization in solution.** *A* and *B*, FCCS analysis of MCL1$_g$ complex with cBID$_r$ (*A*) or cBID$_r^{D95A}$ (*B*) in solution. *Dots*, raw data; *straight lines*, fitted autocorrelation curves (*green* and *red*) and cross-correlation curves (*blue*). Protein concentrations were 250 nM. *C*, percentages of MCL1$_g$·cBID$_r$ and MCL1$_g$·cBID$_r^{D95A}$ complex formation in solution. To estimate the percentage of complex formation, the concentrations of MCL1$_g$, MCL1$_g$·cBID$_r$, and MCL1·cBID$_r^{D95A}$ complexes were obtained from fitted correlation curves as explained under "Experimental Procedures." Data correspond to three independent experiments. *Error bars*, S.E.
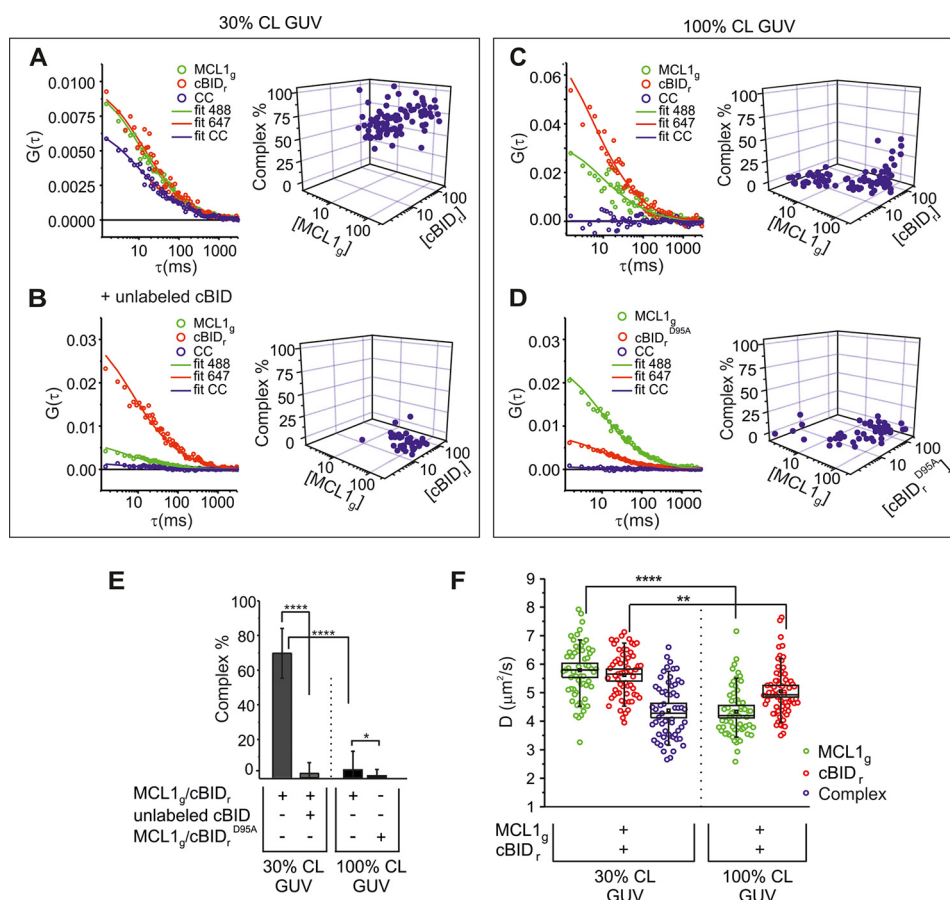

FIGURE 5. **SFCCS analysis indicates that membrane-localized MCL1$_g$ and cBID$_r$ form stable heterodimeric complexes in 30% CL GUV but not in 100% CL GUV.** *A–D*, two-focus SFCCS analysis of MCL1$_g$·cBID$_r$ complex formation in CL-containing GUV. Different concentrations of MCL1$_g$ and cBID$_r$ were incubated with GUV containing 30% CL in the absence (*A*) or presence of unlabeled cBID (*B*). In experiments with 100% CL GUV, MCL1$_g$ was incubated with cBID$_r$ (*C*) or with cBID$_r^{D95A}$ (*D*). *Left-hand panels*, raw data and fitted auto- and cross-correlation curves for the indicated protein and GUV combinations. In the *right-hand panels*, percentages of complex formation (*Complex* %) were represented on a *three-dimensional plot* as a function of individual protein concentrations (molecules/μm^2). *E*, quantification of the effect elicited by unlabeled cBID or cBID$_r^{D95A}$ on MCL1$_g$·cBID$_r$ complex formation in GUV of the indicated lipid compositions. Data correspond to 3–6 independent experiments, with more than 40 GUV analyzed for each condition. *F*, diffusion coefficients (*D*, μm^2/s) of MCL1$_g$ and cBID$_r$ at the different conditions analyzed. The box chart and raw data (*dots*) representations are as described in Fig. 2*D*. Data were obtained from 3–7 independent experiments, with *n* = 61 for 30% CL GUV and *n* = 63 for 100% CL GUV. In *E* and *F*, *, **, and ****, p = 0.05–0.01, 0.01–0.001, and <0.0001, respectively. *Error bars*, S.D.

tion to basal levels. From these experiments, we conclude that membrane-localized MCL1$_g$ and cBID$_r$ form high affinity, stable, and reversible complexes in mitochondrial CS-like GUV.

Next, the same type of experiments were performed in 100% CL GUV. Here, also as expected, MCL1$_g$ and cBID$_r$ efficiently localized to the GUV membrane, reflected by the good quality of MCL1$_g$ and cBID$_r$ autocorrelation curves (Fig. 5*C*, *left, green*

and *red lines*). Surprisingly, in this case, the amplitude of the cross-correlation curve was negligible (Fig. 5*C*, *left*, *blue line*). Thus, despite MCL1$_g$ and cBID$_r$ effectively localizing to the membrane of pure CL GUV, the two proteins do not stably heterodimerize therein. Analyzing cross-correlation percentages in 100% CL GUV treated with a wide range of protein concentrations revealed a measurable amount of MCL1$_g$·cBID$_r$ complex formation at the highest protein concentrations tested (Fig. 5*C*, *three-dimensional plot* at the *right*). The MCL1$_g$·cBID$_r$ complexes detected at such high protein concentrations were not an artifactual result, because the cross-correlation percentage returned to background levels when cBID was substituted by the MCL1 binding-defective cBID$_r^{D95A}$ variant (Fig. 5, *D* and *E*).

Finally, from the autocorrelation and cross-correlation curves, we estimated *D* and hydrodynamic radius (R_H) values for each protein. In solution, *D* values for cBID$_r$, cBID$_r^{D95A}$, and MCL1$_g$ were 92.5 ± 8.7, 91.9 ± 8.3, and 113.8 ± 6.7 μm^2/s, respectively, with corresponding R_H values of 2.37 ± 0.2, 2.38 ± 0.2, and 1.92 ± 0.1 nm, respectively. These values are in accordance with molecular sizes determined for cBID and for MCL1 by NMR spectroscopy and x-ray crystallography (Fig. 1*A*). In 30% CL GUV, MCL1$_g$ and cBID$_r$ displayed virtually identical *D* values around 5.7 μm^2/s, whereas MCL1$_g$·cBID$_r$ complexes showed significantly lower *D* values (4.3 ± 0.8 μm^2/s) (Fig. 5*F*). These *D* values also appear reasonable for membrane-associated proteins and protein complexes. Remarkably, MCL1$_g$ displayed substantially lower *D* values in 100% CL GUV than in 30% CL GUV (Fig. 5*F*). These data suggest that in the presence of membrane-bound cBID$_r$, MCL1$_g$ adopts different conformations in mitochondrial CS-like GUV and in pure CL GUV, which is in accord with the results obtained in alkali extractability experiments using equivalent LUV-type liposomes (Fig. 3*E*). Nevertheless, the possibility cannot be excluded that the alterations in *D* could be due to changes in membrane viscosity induced by different CL contents.

Minimalist Systems Reveal Similarities and Differences between Membrane Interaction modes of BAK$_g$ and MCL1$_g$— Next, we examined the capacity of the BCL2-like structural fold of BAK for membrane association and for heterodimerization with cBID, using the same experimental strategy described above for MCL1.

First, we quantitatively analyzed the binding of BAK$_g$ to high curvature SUV and to low curvature GUV containing different amounts of CL, in the presence and absence of cBID. BAK$_g$ on its own bound quite efficiently to pure CL SUV/GUV, more modestly to mitochondrial CS-like SUV, and insignificantly to CS-like GUV and to MOM-like SUV/GUV (Fig. 6, *A–C*) (data not shown). Thus, high membrane CL content and curvature promote binding of BAK$_g$ on its own to liposomal membranes, which is in qualitative agreement with the behavior observed with MCL1$_g$. Furthermore, cBID$_r$ stimulated BAK$_g$ binding to MOM-like SUV and to CS-like SUV/GUV but not to MOM-like GUV, also matching the behavior observed with MCL1$_g$ (compare Figs. 6 and 2).

Further experiments using heterodimerization-defective mutants of cBID and BAK supported the implication of a canonical BH3-into-groove interaction mechanism in cBID$_r$-

mediated stimulation of BAK$_g$·liposome binding, as observed with MCL1$_g$ (Fig. 7, *A–C*). Nevertheless, the behaviors of BAK$_g$ and MCL1$_g$ were not identical because the cBID D95A mutation inhibited to a lower degree BAK$_g$·liposome binding relative to MCL1$_g$·liposome binding (compare Fig. 7, *B* and *C*, with Fig. 3, *B–D*). Alkali extractability experiments revealed another clear distinction between the membrane-interacting properties of BAK$_g$ and MCL1$_g$, because BAK$_g$ resisted alkaline extraction under all conditions examined (Fig. 7*D*).

*BAK$_g$ and cBID$_r$ Do Not Form Stable Heterodimeric Complexes in CS-like GUV or in Pure CL GUV—*Next, we analyzed BAK$_g$ and cBID$_r$ heterodimerization at the membrane level using SFCCS. As shown in Fig. 8, minimal BAK$_g$·cBID$_r$ heterodimerization was observed either in 30% CL GUV or in 100% CL GUV. Thus, despite the fact that cBID$_r$ efficiently recruits BAK$_g$ to the membrane of these two types of GUV, BAK$_g$ and cBID$_r$ do not form stable heterodimeric complexes therein.

We also estimated *D* values for BAK$_g$ associated with either 30% CL GUV or 100% CL GUV in the presence of cBID$_r$. Similar *D* values were obtained for BAK$_g$ in both types of liposomes (Fig. 8*D*). These results together with those obtained in alkali extractability assays (Fig. 7*D*) suggest, but do not prove, that BAK$_g$ adopts similar conformations in mitochondrial CS-like membranes and in pure CL membranes, which is unlike the behavior observed with MCL1$_g$.

*FRET-based Analysis of MCL1·cBID and BAK·cBID Heterodimerization at the Membrane Level—*We performed FRET experiments to further evaluate the ability of BCL2-like structural folds of MCL1 and BAK to form stable heterodimeric complexes with cBID at the membrane level. To this aim, the same monocysteine MCL1/BAK (donor) and cBID (acceptor) variants used in the previous experiments were labeled either with NBD (donor) or with Rho (acceptor) fluorescent dyes. The fluorescence emission spectrum of NBD overlaps with the absorbance spectrum of Rho, making these two fluorophores a convenient donor-acceptor pair with a relatively large R_0 of ~6 nm (37). We incubated donor and donor plus acceptor samples in solution or with SUV/LUV containing different CL amounts, followed by monitorization of the NBD fluorescence emission spectrum. FRET manifests as a decrease in donor emission (~540 nm) and an increase in acceptor emission (~580 nm) and can be quantified by calculating the ratio of donor plus acceptor fluorescence to donor fluorescence alone (28). A similar experimental strategy has been successfully used before to detect BAX·cBID heterodimerization (26).

Among all samples examined, the most prominent FRET-based interaction signal between MCL1-NBD and cBID-Rho corresponded to the mixture containing 30% CL LUV (Fig. 9, *A* and *B*). This is consistent with the robust MCL1$_g$·cBID$_r$ cross-correlation signal observed in 30% CL GUV by SFCCS (Fig. 5*A*). By contrast, insignificant FRET was detected for the NBD-MCL1·Rho-cBID pair in the presence of 0% CL LUV (Fig. 9, *A* and *B*), which is expected because MCL1$_g$ and cBID$_r$ did not bind to this type of liposome according to the liposome float-up assay (Fig. 2*B*). Minimal FRET signal was also detected when NBD-MCL1 was mixed with Rho-cBID plus 100% CL LUV/SUV (Fig. 9*B*), in agreement with FCCS-based data obtained
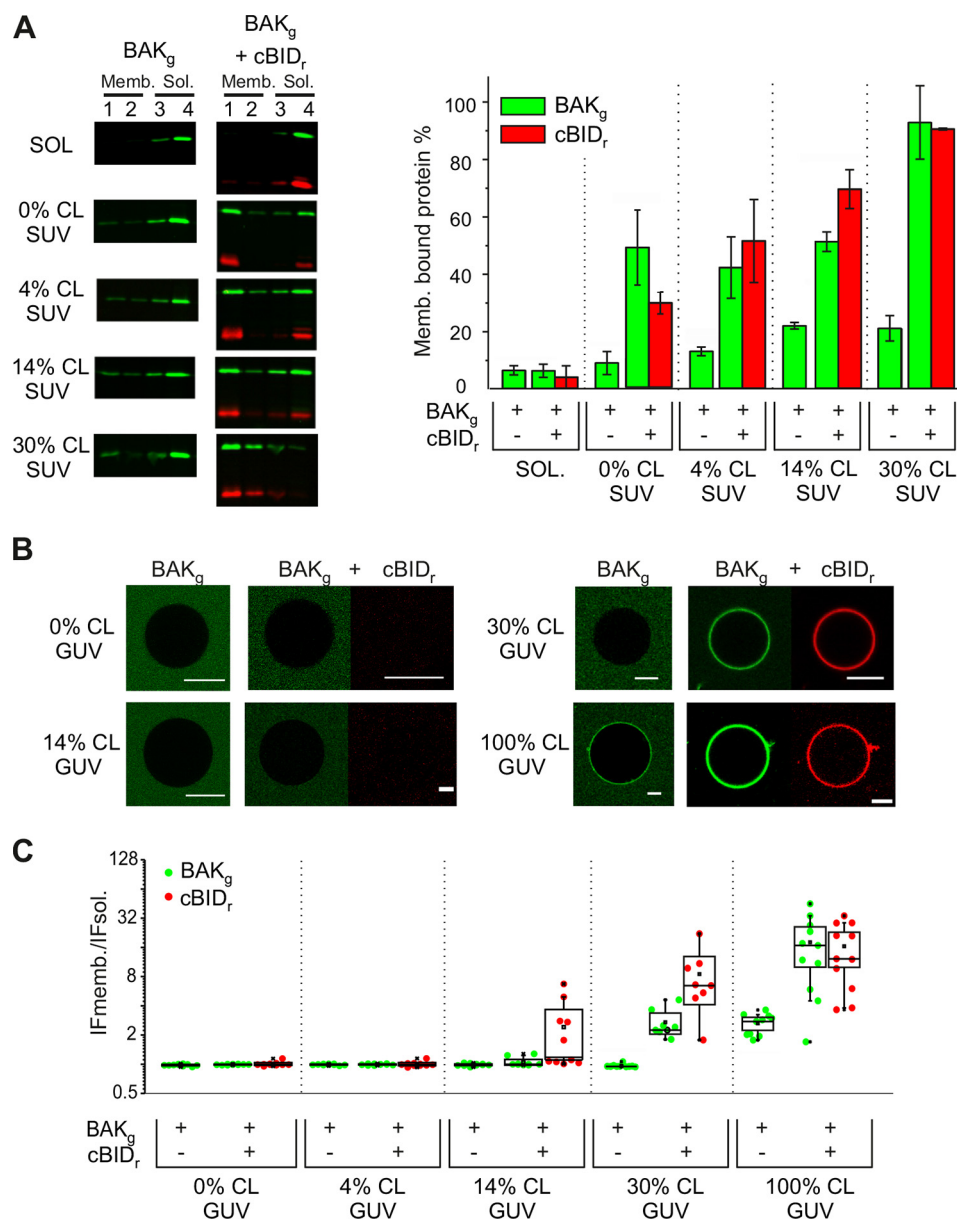
FIGURE 6. **cBID$_r$, CL, and curvature promote BAK$_g$ binding to liposomal membranes.** *A*, BAK$_g$ alone (250 nM) or together with cBID$_r$ (250 nM) was incubated in the absence (*SOL.*) or presence of SUV-type liposomes (250 μM) containing different amounts of CL. Other conditions were as explained in the legend to Fig. 2*A*. *B*, representative images of BAK$_g$ recruitment to GUV containing different amounts of CL, in the absence or presence of cBID$_r$. BAK$_g$ and cBID$_r$ concentrations were 200 and 50 nM, respectively (30% CL GUV assays), and 200 and 20 nM (100% CL GUV assays). Other conditions were as explained in Fig. 2*C*. *C*, from the confocal images, the extents of BAK$_g$ and cBID$_r$ binding to GUV were measured as described in the legend to Fig. 2*D*. *Error bars*, S.D.

with 100% CL GUV (Fig. 5*C*). Importantly, substantial FRET signal was obtained in mixtures containing 0% CL SUV or 30% CL SUV, indicating that NBD-MCL1 and Rho-cBID assemble into stable heterodimeric complexes in MOM-like liposomes and in mitochondrial CS-like liposomes possessing high membrane geometrical curvature (Fig. 9, *A* and *B*). Of note, the degree of FRET was clearly inferior in 30% CL high curvature SUV to that in 30% CL low curvature LUV (Fig. 9, *A* and *B*).

Last, we used this FRET-based assay to evaluate the interaction between the BCL2-like structural fold of BAK and cBID in the presence of different types of liposomes. In stark contrast with results obtained with the NBD-MCL1·Rho-cBID pair, virtually no FRET signal was detected for the NBD-BAK·Rho-

cBID pair under any condition examined (Fig. 9, *C* and *D*). These results strongly suggest that NBD-BAK does not form stable complexes with Rho-cBID, irrespective of membrane CL content and geometrical curvature.

Discussion

Understanding the role of the MOM environment in the function of the BCL2 protein family is one of the most demanding and challenging tasks of current apoptosis research (1–4). In this work, we used multiple fluorescence-based techniques and minimalist model systems to advance our understanding of MCL1 and BAK membrane activities. We report that BCL2-like structural folds of MCL1 and BAK lacking the MA domain display membrane interaction
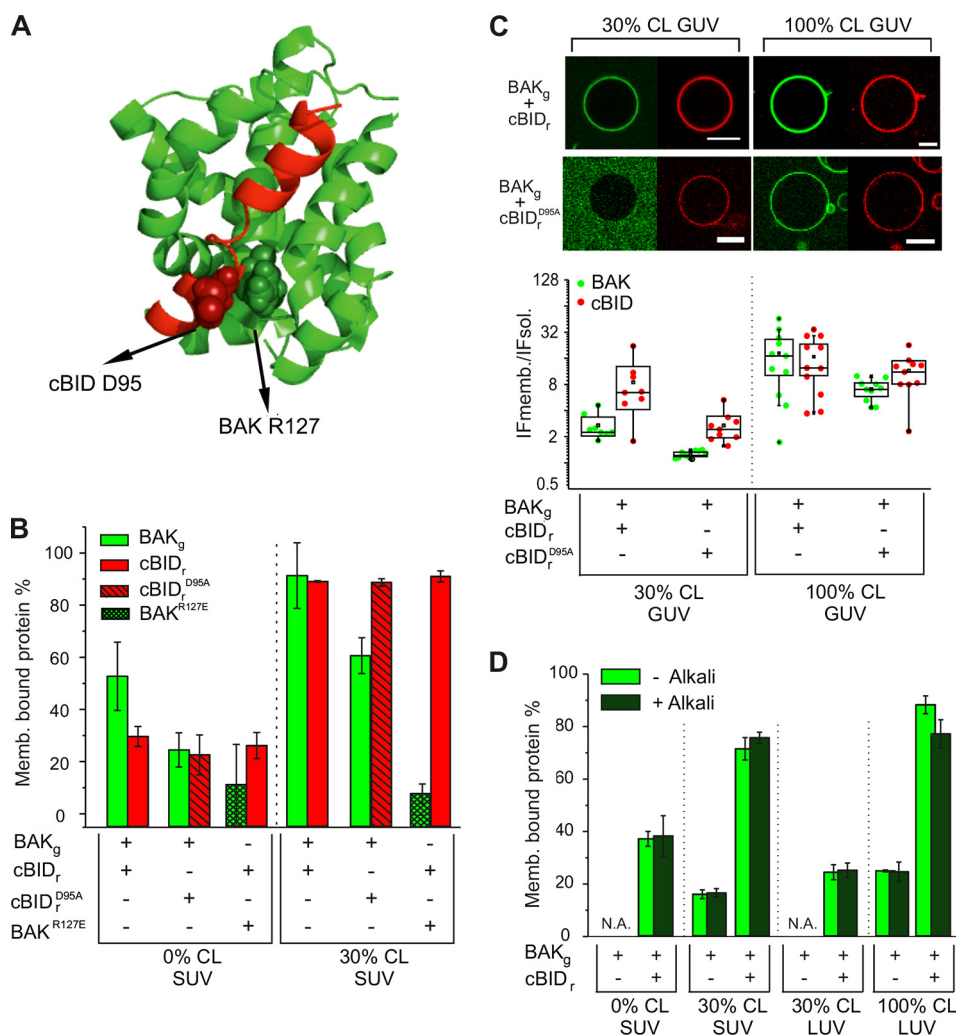
FIGURE 7. **Different membrane association modes of BAK$_g$.** *A,* structural representation of BID SAHB BH3 domain (*red*) bound to BAKΔC21 (*green*), highlighting as *spheres* cBID Asp[95] and BAK Arg[127] residues implicated in BID BH3-BAK groove interaction (PDB code 2M5B). *B* and *C,* effect of cBID$_r^{D95A}$ and BAK^{R127E} mutations on protein binding to liposomes containing different amounts of CL. cBID$_r^{D95A}$ recruitment to SUV and GUV was assessed as described in Fig. 3, *B–D,* whereas BAK^{R127E} recruitment to liposomes was assessed by immunoblotting and densitometric quantification. BAK$_g$ and cBID$_r$ concentrations were 250 and 250 nM, respectively, in assays with SUV, 200 and 50 nM in assays with 30% CL GUV, and 200 and 20 nM in assays with 100% CL GUV. *D,* alkali extractability assay. Proteins incubated with liposomes were treated with (+*Alkali*) or without (−*Alkali*) (100 mM Na$_2$CO$_3$, pH 11.5), and their partition was assessed as described in Fig. 2, *A* and *B. Error bars,* S.D.

modes sharing certain similarities but also displaying important differences.

Recent studies indicate that the localization of multiple BCL2 family proteins (including MCL1 and BAK) at the MOM is more dynamic than previously anticipated and depends on the physiological status of the cell, with these proteins continuously being retrotranslocated from the MOM into the cytosol under healthy conditions, whereas apoptotic stimulation leads to general accumulation of BCL2 family proteins at the MOM (1, 3, 4). It is becoming clear that retrotranslocation processes taking place under non-apoptotic conditions are governed by heterodimerizing interactions between BCL2-type and BAX-type proteins involving their C-terminal MA domains (14–18). However, how BCL2 family proteins become generally accumulated at the MOM downstream of apoptosis triggering remains poorly understood, although different lines of evidence indicate that BCL2-like structural folds of multi-BH motif BCL2 family proteins can be implicated in this process (9, 11, 12, 13). Here, we used model membrane systems to evaluate

whether three distinct apoptosis-related factors (cBID, CL, and membrane geometrical curvature) affect membrane recruitment of BCL2-like structural folds belonging to MCL1 and to BAK as well as to gain more mechanistic insight into each one of these processes.

Regarding cBID, we found that this apoptogenic BH3-only protein promotes membrane recruitment of the BCL2-like structural fold of MCL1 through a canonical BH3-into-groove interaction mechanism, which has been extensively characterized in solution-based studies (1). A similar, although apparently not identical, protein-protein interaction mechanism also accounts for cBID-mediated membrane recruitment of the BCL2-like structural fold of BAK. These data are consistent with the "membrane-embedded" model for BCL2 protein family action stating that upon apoptosis triggering, mitochondria-associated BH3-only proteins can act as receptors for recruiting BAX-type and BCL2-type proteins into the MOM (4, 25, 26). Of note, we also showed that interaction with cBID$_r$ triggers membrane insertion of BAK$_g$ but not MCL1$_g$. This is in contrast with
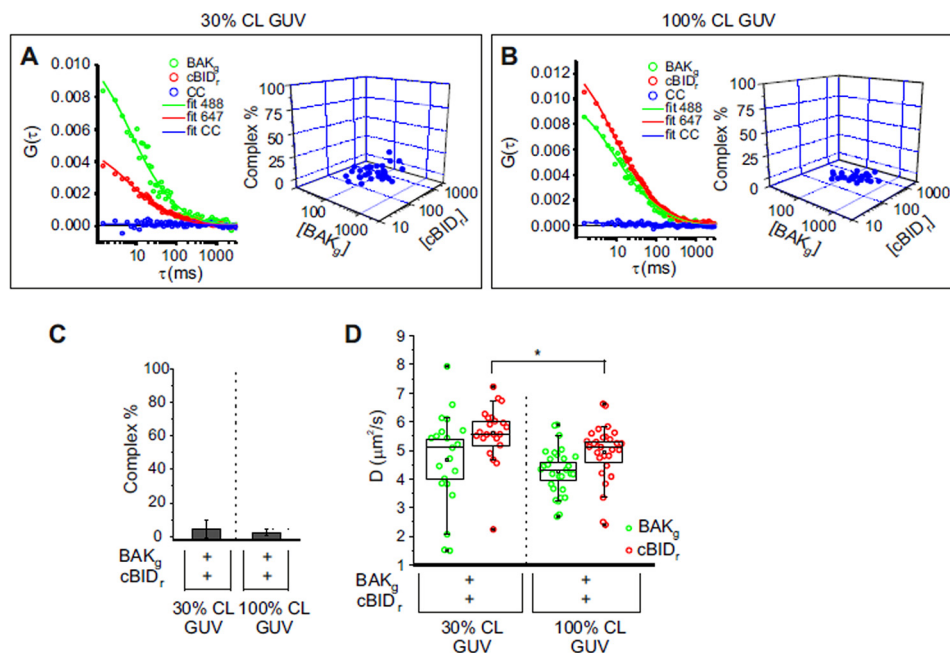
FIGURE 8. **SFCCS analysis indicates that membrane-localized BAK_g and $cBID_r$ do not form stable heterodimeric complexes in CL-containing GUV.** *A* and *B*, two-focus SFCCS analysis of $BAK_g \cdot cBID_r$ complex formation in GUV containing 30% CL (*A*) or 100% CL (*B*). Panels are as described in the legend to Fig. 5, *A–D*. *C*, quantification of complex formation of $BAK_g \cdot cBID_r$ in 30% CL GUV and in 100% CL GUV. Data correspond to 2–3 independent experiments, with more than 25 GUV analyzed for each condition. *D*, diffusion coefficients (*D*) of BAK_g and $cBID_r$ at the different conditions analyzed. The box chart and raw data (*dots*) representations are as described in the legend to Fig. 2D. Data were obtained from 2–5 independent experiments, with $n = 29$ for 30% CL GUV, and $n = 35$ for 100% CL GUV. *, $p = 0.05–0.01$. *Error bars*, S.D.

another prediction of the "membrane-embedded" model stating that interaction with BH3-only proteins triggers membrane embedding of the $\alpha5\alpha6$ region of BCL2-type proteins, which subsequently functions as a non-canonical surface for binding to and inhibiting BAX-type proteins (4). The latter proposal originated from observations made with BCL2 (11), but it remains to be proven that this phenomenon can be extended to BCL2-type proteins other than BCL2 itself.

Concerning CL, we showed that this mitochondrion-specific lipid also promotes liposome association of BCL2-like structural folds corresponding to both MCL1 and BAK. Although the physiological relevance of the latter set of results can be put into question due to the high CL amounts required to observe such effects, recent studies indicate that CL and its derivatives become enriched at the MOM early during the apoptotic process (34, 35). Interestingly, further evidence indicates that lipids other than CL accumulate at the MOM during apoptosis and interact selectively with specific BCL2 family members (22).

Last, our studies also revealed that high geometrical curvature promotes membrane association of BCL2-like structural folds belonging to both MCL1 and BAK. Certain proteins display the ability to sense membrane geometrical curvature through their intrinsic shape (38), but BCL2-like structural folds of MCL1 and BAK are not intrinsically curved. On the other hand, all multi-BH motif BCL2 family members contain amphipathic helices with potential for sensing membrane geometrical curvature by inserting within curvature-created lipid packing defects (38). Of note, specific lipids and curvature-created lipid packing defects are both increasingly recognized as contributing factors in membrane relocalization events involving not only cytosolic proteins translocating to intracellular

membranes, but also membrane-integrated proteins relocalizing within specialized membrane regions (*i.e.* intramembrane protein sorting) (39–41).

Based on these collective observations, it is tempting to speculate that MOM-localized BH3-only proteins, specific MOM lipids, and MOM geometrical curvature can all contribute to mitochondrial accumulation of multi-BH motif BCL2 family proteins observed in the course of the apoptotic process. Nevertheless, it is clear that further experiments with cellular systems are required to test the validity of this hypothesis.

Another important finding of our study is the identification of two different ways by which membrane association affects MCL1·cBID complex formation. On the one hand, our SFCCS and FRET results indicate that, relative to the situation found in solution, the likelihood of MCL1·cBID heterodimerization increases severely in the presence of mitochondrial CS-like GUV/LUV and less prominently in the presence of mitochondrial CS-like SUV. Based on previous observations, it is likely that liposomes with a mitochondrial CS-like membrane composition generally stimulate MCL1·cBID complex formation by triggering exposure of the cBID BH3 motif (42, 43). However, why is the level of MCL1·cBID heterodimerization higher in mitochondrial CS-like GUV/LUV than in mitochondrial CS-like SUV? We note that the alkali-extractable fraction of $MCL1_g$ is notably larger in the former low curvature liposomes than in the latter high curvature vesicles (Fig. 3*E*). On the one hand, $MCL1_g$ may adopt a peripheral membrane-adsorbed conformation in low curvature CS-like LUV/GUV that preserves the BH3-binding groove of the molecule intact and thereby maximizes $MCL1_g \cdot cBID_r$ heterodimerization. On the other hand, partial membrane insertion of $MCL1_g$ in high cur-
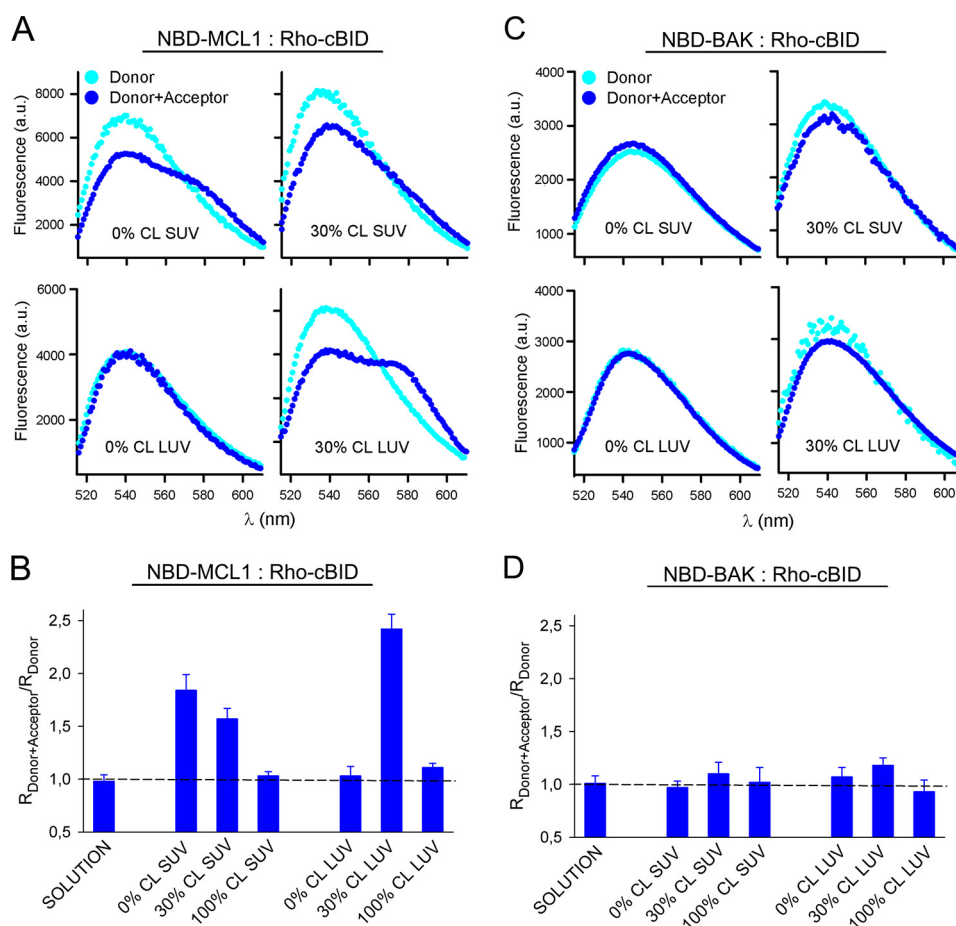
FIGURE 9. **FRET-based assessment of MCL1·cBID and BAK·cBID complex formation in liposomal membranes.** *A* and *B*, assessment of FRET between NBD-MCL1 (donor) and Rho-cBID (acceptor) in the presence of different types of liposomes. *C* and *D*, assessment of FRET between NBD-BAK (donor) and Rho-cBID (acceptor) in the presence of different types of liposomes. Net emission spectra were used for calculation of FRET signals in *B* and *D*, with data reflecting mean values ± S.E. (*error bars*) (n = 3–5). For further details, see "Experimental Procedures."

vature CS-like SUV may alter the BH3-binding groove of $MCL1_g$ in a manner that diminishes $cBID_r$ binding. Following the same rationale, minimal $MCL1_g \cdot cBID_r$ heterodimerization detected in CL SUV, LUV, and GUV could be explained by destruction of the BH3-binding groove of $MCL1_g$ due to extensive integration of the protein into pure CL liposomal membranes. Alternatively, or in addition, high membrane geometrical curvature and/or CL content may cause membrane insertion and hindering of the $cBID_r$ BH3 motif. In fact, it has been reported that cBID inserts the hydrophobic face of its BH3 motif into the hydrophobic interior of highly curved anionic micelles (43).

Independently of these open questions, our findings raise the exciting possibility that MCL1 heterodimerization with other BCL2 family partners could be dynamically modulated by changes in lipid composition and/or geometrical curvature occurring at localized sites of the MOM. Furthermore, it can be hypothesized that changes in mitochondrial membrane lipid composition or geometrical curvature may affect MCL1 interaction with non-BCL2 family partners (44, 45). In this context, we propose that mitochondrial membrane lipid composition and geometrical curvature should be considered as "active" parameters in the BCL2 family interactome, in the sense that they could contribute to the self-organization of reactions between BCL2 family members at the MOM level.

Interaction between BAK and cBID is commonly described as a transient "hit-and-run" process, mainly to account for the observation that despite the fact that cBID triggers functional BAK activation, cBID does not form complexes with BAK in detergent-solubilized mitochondrial membrane extracts (1, 3, 4). However, it remained unproven whether this is a property displayed by the BAK molecule in an unperturbed lipid bilayer membrane environment. Our SFCCS and FRET results now show that the BCL2-like structural fold of BAK does not form a stable complex with cBID in a mitochondrial-like lipid bilayer membrane environment. The molecular details of this phenomenon remain to be fully elucidated. Nevertheless, based on our own results as well as observations made by other groups, a likely scenario is as follows (1, 10, 46): (i) initially, membrane-bound cBID and BAK heterodimerize through a canonical BH3-into-groove mechanism; (ii) this event destabilizes the BAK solution fold, leading to disengagement of BID BH3 from the BAK groove and exposure of the BAK BH3 motif; (iii) the exposed BAK BH3 motif engages into the groove of another BAK molecule to form a stable BAK homodimer. One important question remaining is why cBID-BAK interaction is more destabilizing than cBID-MCL1 interaction at the membrane level. Another prominent question remaining is whether the manifold membrane interaction modes described here for the BCL2-like structural folds of MCL1, BAK, and cBID can be

extended to other BCL2 family members. The reconstituted systems and techniques described in this study may provide powerful tools with which to continue elucidating important mechanistic aspects of BCL2 family proteins, particularly in the context of a lipid bilayer membrane milieu.

References

1. Czabotar, P. E., Lessene, G., Strasser, A., and Adams, J. M. (2014) Control of apoptosis by the BCL2 protein family: implications for physiology and therapy. *Nat. Rev. Mol. Cell Biol.* **15,** 49–63
2. Basañez, G., Soane, L., Hardwick, J. M. (2012) A new view of the lethal apoptotic pore. *PLoS Biol.* **10,** e1001399
3. Westphal, D., Kluck, R. M., and Dewson, G. (2014) Building blocks of the apoptotic pore: how Bax and Bak are activated and oligomerize during apoptosis. *Cell Death Differ.* **21,** 196–205
4. Shamas-Din, A., Kale, J., Leber, B., and Andrews DW (2013) Mechanisms of action of Bcl-2 family proteins. *Cold Spring Harb. Perspect. Biol.* **5,** a008714
5. Aouacheria, A., Rech de Laval, V., Combet, C., and Hardwick, J. M. (2013) Evolution of Bcl-2 homology motifs: homology *versus* homoplasy. *Trends Cell Biol.* **23,** 103–111
6. Lutter, M., Fang, M., Luo, X., Nishijima, M., Xie, X., and Wang, X. (2000) Cardiolipin provides specificity for targeting of tBid to mitochondria. *Nat. Cell Biol.* **2,** 754–761
7. Nouraini, S., Six, E., Matsuyama, S., Krajewski, S., and Reed J.C. (2000) The putative pore-forming domain of Bax regulates mitochondrial localization and inreraction with Bcl-XL. *Mol. Cell. Biol.* **20,** 1604–1615
8. Priault, M., Cartron, P.-F., Camougrand, N., Antonsson, B., Vallette, F. M., and Manon, S. (2003) Investigation of the role of the C-terminus of Bax and of tc-Bid on Bax interaction with yeat mitochondria. *Cell Death Differ.* **10,** 1068–1077
9. Valentijn, A.J., Upton, J.-P., Bates, N., and Gilmore, A. P. (2008) Bax targeting to mitochondria occurs via both tail anchor-dependent and -independent mechanisms. *Cell Death Differ.* **15,** 1243–1254
10. Brouwer, J. M., Westphal, D., Dewson, G., Robin, A. Y., Uren, R. T., Bartolo, R., Thompson, G. V., Colman, P. M., Kluck, R. M., and Czabotar, P. E. (2014) Bak core and latch domains separate during activation, and freed core domains form symmetric homodimers. *Mol. Cell* **55,** 938–946
11. Kim, P. K., Annis, M. G., Dlugosz, P. J., Leber, B., and Andrews, D. W. (2004) During apoptosis bcl-2 changes membrane topology at both the endoplasmic reticulum and mitochondria. *Mol. Cell* **14,** 523–529
12. George, N. M., Targy, N., Evans, J. J. D., Zhang, L., and Luo, X. (2010) Bax contains two functional mitochondrial targeting sequences and translocates to mitochondria in a conformational change- and homo-oligomerization-driven process. *J. Biol. Chem.* **285,** 1384–1392
13. Nakajima, W., Hicks, M. A., Tanaka, N., Krystal, G. W., and Harada, H. (2014) Noxa determines localization and stability of MCL1 and consequently ABT-737 sensitivity in small cell lung cancer. *Cell Death Dis.* **5,** e1052
14. Edlich, F., Banerjee, S., Suzuki, M., Cleland, M. M., Arnoult, D., Wang, C., Neutzner, A., Tjandra, N., and Youle, R. J. (2011) Bcl-x(L) retrotranslocates Bax from the mitochondria into the cytosol. *Cell* **145,** 104–116
15. Schellenberg, B., Wang, P., Keeble, J. A., Rodriguez-Enriquez, R., Walker, S., Owens, T. W., Foster, F., Tanianis-Hughes, J., Brennan, K., Streuli, C. H., and Gilmore A. P. (2013) Bax exists in a dynamic equilibrium between the cytosol and mitochondria to control apoptotic priming. *Mol. Cell* **49,** 959–971
16. Todt, F., Cakir, Z., Reichenbach, F., Youle, R. J., and Edlich, F. (2013) The C-terminal helix of Bcl-x(L) mediates Baxretrotranslocation from the mitochondria. *Cell Death Differ.* **20,** 333–342
17. Todt, F., Cakir, Z., Reichenbach, F., Emschermann, F., Lauterwasser, J., Kaiser, A., Ichim, G., Tait, S. W., Frank, S., Langer, H. F., Edlich, F. (2015) Differential retrotranslocation of mitochondrial Bax and Bak. *EMBO J.* **34,** 67–80
18. Renault, T. T., Teijido, O., Missire, F., Ganesan, Y. T., Velours, G., Arokium, H., Beaumatin, F., Llanos, R., Athané, A., Camougrand, N., Priault, M., Antonsson, B., Dejean, L. M., and Manon, S. (2015) Bcl-xl stim-

19. Montessuit, S., Somasekharan, S. P., Terrones, O., Lucken-Ardjomande, S., Herzig, S., Schwarzenbacher, R., Manstein, D. J., Bossy-Wetzel, E., Basañez, G., Meda, P., and Martinou, J. C. (2010) Membrane remodeling induced by the dynamin-related protein Drp1 stimulates Bax oligomerization. *Cell* **142,** 889–901
20. Landeta, O., Landajuela, A., Gil, D., Taneva, S., Di Primo, C., Sot, B., Valle, M., Frolov, V. A., Basañez, G. (2011) Reconstitution of proapoptotic BAK function in liposomes reveals a dual role for mitochondrial lipids in the BAK-driven membrane permeabilizationprocess. *J. Biol. Chem.* **286,** 8213–8230
21. Landeta, O., Garcia Valero, J., Flores-Romero, H., Bustillo-Zabalbeitia, I., Landajuela, A., Garcia-Porras, M., Terrones, O., and Basañez, G. (2014) Lipid-dependent bimodal MCL1 membrane activity. *ACS Chem. Biol.* **9,** 2852–2863
22. Renault, T. T., and Chipuk, J. E. (2014) Death upon a kiss: mitochondrial outer membrane composition and organelle communication govern sensitivity to BAK/BAX-dependent apoptosis. *Chem. Biol.* **21,** 114–123
23. Renault, T. T., Floros, K. V., Elkholi, R., Corrigan, K. A., Kushnareva, Y., Wieder, S. Y., Lindtner, C., Serasinghe, M. N., Asciolla, J. J., Buettner, C., Newmeyer, D. D., and Chipuk, J. E. (2015) Mitochondrial shape governs BAX-induced membrane permeabilization and apoptosis. *Mol. Cell* **57,** 69–82
24. Terrones, O., Antonsson, B., Yamaguchi, H., Wang, H. G., Liu, J., Lee, R. M., Herrmann, A., and Basañez, G. (2004) Lipidic pore formation by the concerted action of proapoptotic BAX and tBID. *J. Biol. Chem.* **279,** 30081–30091
25. Billen, L. P., Kokoski, C. L., Lovell, J. F., Leber, B., and Andrews, D. W. (2008) Bcl-XL inhibits membrane permeabilization by competing with Bax. *PLoS Biol.* **6,** e147
26. Lovell, J. F., Billen, L. P., Bindner, S., Shamas-Din, A., Fradin, C., Leber, B., and Andrews, D. W. (2008) Membrane binding by tBid initiates an ordered series of events culminating in membrane permeabilization by Bax. *Cell* **135,** 1074–1084
27. Bleicken, S., Landeta, O., Landajuela, A., Basañez, G., García-Sáez, A. J. (2013) Proapoptotic Bax and Bak proteins form stable protein-permeable pores of tunable size. *J. Biol. Chem.* **288,** 33241–33252
28. Burré, J., Sharma, M., Südhof, T. C. (2014) α-Synuclein assembles into higher-order multimers upon membrane binding to promote SNARE complex formation. *Proc. Natl. Acad. Sci. U.S.A.* **111,** E4274–E4283
29. He, L., Perkins, G. A., Poblenz, A. T., Harris, J. B., Hung, M., Ellisman, M. H., and Fox, D. A. (2003) Bcl-xl overexpression blocks bax-mediated mitochondrialcontact site formation and apoptosis in rod photoreceptors of lead-exposed mice. *Proc. Natl. Acad. Sci. U.S.A.* **100,** 1022–1027
30. Sano, R., Annunziata, I., Patterson, A., Moshiach, S., Gomero, E., Opferman, J., Forte, M., and d'Azzo, A. (2009) GM1-ganglioside accumulation at the mitochondria-associated ER membranes links ER stress to Ca^{2+}-dependent mitochondrial apoptosis. *Mol. Cell* **36,** 500–511
31. Martinou, J. C., and Youle, R. J. (2011) Mitochondria in apoptosis: Bcl-2 family members and mitochondrial dynamics. *Dev. Cell.* **21,** 92–101
32. Horvath, S. E., and Daum, G. (2013) Lipids of mitochondria. *Prog. Lipid Res.* **52,** 590–614
33. Renner, L. D., and Weibel, D. B. (2011) Cardiolipinmicrodomains localize to negatively curved regions of *Escherichia coli* membranes. *Proc. Natl. Acad. Sci. U.S.A.* **108,** 6264–6269
34. Chu, C. T., Ji, J., Dagda, R. K., Jiang, J. F., Tyurina, Y. Y., Kapralov, A. A., Tyurin, V. A., Yanamala, N., Shrivastava, I. H., Mohammadyani, D., Qiang-Wang, K. Z., Zhu, J., Klein-Seetharaman, J., Balasubramanian, K., Amoscato, A. A., Borisenko, G., Huang, Z., Gusdon, A. M., Cheikhi, A., Steer, E. K., Wang, R., Baty, C., Watkins, S., Bahar, I., Bayır, H., and Kagan, V. E. (2013) Cardiolipin externalization to the outer mitochondrial membrane acts as an elimination signal for mitophagy in neuronal cells. *Nat. Cell Biol.* **15,** 1197–1205
35. Tyurina, Y. Y., Poloyac, S. M., Tyurin, V. A., Kapralov, A. A., Jiang, J., Anthonymuthu, T. S., Kapralova, V. I., Vikulina, A. S., Jung, M. Y., Epperly, M. W., Mohammadyani, D., Klein-Seetharaman J., Jackson, T. C., Kochanek, P. M., Pitt, B. R., Greenberger, J. S., Vladimirov, Y. A., Bayır, H.,

and Kagan, V. E. (2014) A mitochondrial pathway for biosynthesis of lipid mediators. *Nat. Chem.* **6,** 542–552

36. Hermann, E., Ries, J., and García-Sáez, A. J. (2015) Scanning fluorescence correlation spectroscopy in biomembranes. *Methods Mol. Biol.* **1232,** 181–197

37. Turcatti, G., Nemeth, K., Edgerton, M. D., Meseth, U., Talabot, F., Peitsch, M., Knowles, J., Vogel, H., and Chollet, A. (1996) Probing the structure and function of the tachykinin neurokinin-2 receptor through biosynthetic incorporation of fluorescent amino acids at specific sites. *J. Biol. Chem.* **271,** 19991–19998

38. Kozlov, M. M., Campelo, F., Liska, N., Chernomordik, L. V., Marrink, S. J., and McMahon, H. T. (2014) Mechanisms shaping cell membranes. *Curr. Opin. Cell Biol.* **29,** 53–60

39. Bigay, J., and Antonny, B. (2012) Curvature, lipid packing, and electrostatics of membrane organelles: defining cellular territories in determining specificity. *Dev. Cell.* **23,** 886–895

40. Vanni, S., Hirose, H., Barelli, H., Antonny, B., and Gautier, R. (2014) A sub-nanometre view of how membrane curvature and composition modulate lipid packing and protein recruitment. *Nat. Commun.* **5**, 4916

41. Aimon, S., Callan-Jones, A., Berthaud, A., Pinot, M., Toombes, G. E., and Bassereau, P. (2014) Membrane shape modulates transmembrane protein distribution. *Dev. Cell.* **28,** 212–218

42. Shamas-Din, A., Bindner, S., Zhu, W., Zaltsman, Y., Campbell, C., Gross, A., Leber, B., Andrews, D. W., and Fradin, C. (2013) tBid undergoes multiple conformational changes at the membrane required for Bax activation. *J. Biol. Chem.* **288,** 22111–22127

43. Wang, Y., and Tjandra, N. (2013) Structural insights of tBid, the caspase-8-activated Bid, and its BH3 domain. *J. Biol. Chem.* **288,** 35840–35851

44. Perciavalle, R. M., and Opferman, J. T. (2013) Delving deeper: MCL-1's contributions to normal and cancer biology. *Trends Cell Biol.* **23,** 22–29

45. Hardwick, J. M., and Soane, L. (2013) Multiple functions of BCL-2 family proteins. *Cold Spring Harb. Perspect. Biol.* 10.1101/cshperspect.a008722

46. Moldoveanu, T., Grace, C.R., Llambi, F., Nourse, A., Fitzgerald, P., Gehring, K., Kriwacki, R. W., and Green, D. R. (2013) BID-induced structural changes in BAK promote apoptosis. *Nat. Struct. Mol. Biol.* **20,** 589–597